

Direct-writing of two-dimensional diodes by focused ion beams

Yanran Liu, Yuanyuan Qu, Yue Liu, Hang Yin, Jinglun Liu, Yang Tan, and Feng Chen*,*

Y. Liu, Y. Qu, Y. Liu, H. Yin, Y. Tan, F. Chen

School of Physics, State Key Laboratory of Crystal Materials, Shandong University,
Shandong, Jinan, 250100, China

E-mail: tanyang@sdu.edu.cn; drfchen@sdu.edu.cn

J. Liu

Department of Physics and Electronic Engineering, Heze University, Shandong Heze,
274015, China

Keywords: Focused ion beam writing, 2D heterostructures, graphene, diodes

ABSTRACT

In the past decade, electronic devices based on graphene and the related two-dimensional (2D) materials have exhibited outstanding figures of merit. However, so far, the fabrication of two-dimensional diodes, as elementary building blocks of electronic devices, still relies on manual or semi-automated handling processing. To unleash their commercial potential, the integration of 2D materials into a fully-automated fabrication line is a critical step. Here, we elucidate the focused ion-beam writing as an automated approach to construct lateral diodes on a 2D heterostructure (MoSe_2/G) consisting of the stacked monolayer graphene and MoSe_2 . *Se*-defects generated by focused ion writing endow the 2D heterostructure with unique electronic properties like the adjustable work function and the quasi-metallic state, which allows for the construction of the barrier at the boundary of the writing and non-writing region. Benefiting from this feature, the ion-beam-written heterostructure is used to realize rectifying and current regulating diodes. Exhibiting comparable performance to traditional diodes, the rectifying diode has a rectification ratio of $\sim 10^4$, while the current regulative diode has a dynamic resistance larger than $4.5 \text{ M}\Omega$. Furthermore, to illustrate practical applications of these diodes in digital logic electronics, AND and OR logic gates are directly inscribed on the heterostructure by ion beams. Our work demonstrates the focused ion-beam writing as an additional strategy for direct-writing of 2D diodes on graphene-based heterostructures.

INTRODUCTION

The diode is the rudimentary building block for electronic circuits [1] for applications of logic and filter circuits. With exceptional electronic properties, two-dimensional (2D) materials, such as graphene [2, 3] and transition metal dichalcogenides (TMDCs) [4], have skyrocketed as candidate materials for the future evolution of electronics, attracting immense interests among the electron-device community [5]. Towards this purpose, many approaches for the 2D diode fabrication have been intensively proposed, such as stacking 2D layers with dissimilar charge-carrier types [6-8], hetero-atom doping [9, 10], electrostatic doping, [11, 12] and chemical doping [13, 14]. Nevertheless, these approaches require complete or partial manual operations, considerably limiting their commercial applications. For example, the integration of graphene with semiconductors forms a graphene/semiconductor (G/S) Schottky junction, which is recognized as a promising candidate for real-life applications [15, 16]. Nevertheless, the multiple site-directed transfers of graphene onto the substrate, as the crucial step in the preparation of G/S junctions, lack the benefits of fully-automated manufacturing tools up to now [15, 16]. The manual or semi-automated handling of G/S junctions brings challenges for its widespread applications, such as device reproducibility, fabrication yield, and reliability [16]. Therefore, an approach with a fully-automated or well-established process-line would represent a significant leap forward for the applications of 2D electronic devices [15, 16].

Focused ion beam (FIB) is a highly-automated technique to micromachine the target surface with a high spatial resolution of ~ 10 nm [17, 18]. Commercial FIB systems are characterized by a Ga^+ ion beam with an energy of 30 keV. While being commonly used for milling at a high fluence of Ga^+ ions, the FIB process can also be employed at low fluence to give rise to several effects in 2D materials, such as the introduction of defects in selected regions [19]. Firstly, through controlling specific FIB parameters, the sputtering of target atoms by FIB processing can be limited to the top atomic layer; secondly, atoms are

specifically removed from the target, enabling the defect-pattern on the target surface; and thirdly, defect-engineering (DE) triggered by FIB bombardment is capable of tailoring the electronic properties of materials for desired applications. The above effects are incredibly crucial and attractive for 2D transition metal dichalcogenides (e.g., MoSe_2), which contain three layers of atoms. By using FIB, defects (i.e., *Se*-vacancies through sputtered *Se* atoms) can be introduced locally in the first atomic layer to achieve modification of the electronic structure in a specific micro-region [19-21]. Furthermore, through stacking the defective MoSe_2 onto graphene, it is then possible to engineer Van der Waals heterostructures to be with new electronic structures determined by DE [20, 21].

In this work, we demonstrate that FIB can be used to directly write high-performance 2D diodes on a heterostructure consisted of the stacked monolayer MoSe_2 and graphene. The schematic diagram of FIB-writing of the 2D diode on the MoSe_2/G heterostructure is illustrated in Figure 1. In this prototype, the focused Ga^+ ion beams are utilized to irradiate the MoSe_2 side of the heterostructure, sputtering *Se* atoms from the top atomic layer. *Se*-vacancies transfer the irradiated heterostructure from MoSe_2 -modified graphene to quasi-metallic MoSe_x/G ($x=1.6$ or 1.4), according to the fact whether the Dirac point is present. The contact of $\text{MoSe}_{1.6}/\text{G}$ - MoSe_2/G (or $\text{MoSe}_{1.4}/\text{G}$ - MoSe_2/G) is similar to the graphene-metal contact, generating a p-n junction without the obstacles caused by the Klein tunneling. This work offers a candidate route for the direct-writing of electronic circuits on 2D materials via FIB.

Defect-engineered MoSe_x/G heterostructure

The MoSe₂/G heterostructure with MoSe₂ monolayer on the top is irradiated by a focused Ga⁺ ion beam with energy of 30 keV and fluence between 10¹³ and 10¹⁵ ions/cm². The composition of the heterostructure before and after the FIB-writing is determined through X-ray photoelectron spectroscopy (XPS), as shown in Supplementary I. Before writing, the heterostructure has stoichiometric ratios of Se:Mo = 2, and C:Mo = 12, suggesting the high crystallinity of the as-prepared heterostructure. After irradiation, the integration of the photoemission peak shows a reduction in Se-3d, a slight change in Mo-3d, and a negligible variation in C-1s atoms. This indicates that numerous Se atoms are removed from the top atomic layer, while Mo and C atomic layers remain comparatively unchanged. Figure 2a shows the evolution of the Se:Mo stoichiometric ratio (*x*) as a function of the ion fluence, demonstrating stabilized stoichiometries of MoSe_x (*x* = 2, 1.8, 1.6, and 1.4) in agreement with previous time-resolved ion sputtering study of MoSe₂ [22–24]. The dangling bonds left by sputtered Se atoms are investigated via the comparison of the high-resolution XPS spectra of MoSe_x/G (Mo-3d) in Fig. 2b and 2c. The Mo⁴⁺ peaks of MoSe₂/G locates at 229.2 eV (Mo-3d_{3/2}) and 232.3 eV (Mo-3d_{5/2}), whilst Mo⁶⁺ peaks at ~232.8 eV and ~236.2 eV appear in MoSe_{1.8}/G, MoSe_{1.6}/G and MoSe_{1.4}/G, indicating the generation of dangling bonds of Mo atoms due to Se-vacancies [25]. Figure 2c presents the Raman spectra of MoSe_x/G heterostructures at bands of MoSe_x (A_{1g}) and graphene (D, G, and 2D) normalized by the maximum intensity of the G band. After the FIB irradiation, a second peak associated with Se-vacancies arises adjacent to the A_{1g} peak [26], whilst there is negligible change in D, G, and 2D Raman bands, suggesting the well-preserved graphene.

Figure 2d displays the atomic force microscopy (AFM) and Kelvin probe microscopy (KPFM) images of the two inscribed rectangle shapes in the heterostructure corresponding to MoSe_{1.8}/G and MoSe_{1.4}/G. In the AFM image, the thickness of the whole heterostructure is uniform after the Ga⁺ ion irradiation (Fig. 2e). This means that the amount of Se-vacancies is

not large enough to change the morphology, and only the top atomic layer becomes defective. A visible boundary between the irradiated and pristine areas is observed in the KPFM image (Fig. 2d), and the rectangular imprint becomes even clearer as x decreases. The KPFM image represents the work function (associated with surface potential) of the irradiated heterostructure ($W_{\text{MoSe}_x/\text{G}}$) altered by *Se*-vacancies [27], which has a direct relationship with x , i.e., 5.2 eV for the $\text{MoSe}_{2.0}/\text{G}$, 5.1 eV for $\text{MoSe}_{1.8}/\text{G}$, 5.0 eV for $\text{MoSe}_{1.6}/\text{G}$, and 4.85 eV for $\text{MoSe}_{1.4}/\text{G}$, respectively (Fig. 2f and Supplementary II). This circumstance suggests that DE does not change the morphology but can easily modify the electrical property of the heterostructure.

To detect the transport characteristics of the defect-engineered heterostructure, we fabricate top-gated field-effect transistors (FETs) based on the MoSe_x/G . For x equal to 2 and 1.8 (Fig. 3a and 3c), MoSe_x/G based FETs exhibit the typical ambipolar transport behavior with the Dirac point shifted from the gate voltage of -2.0 V ($x = 2$) to 1.5 V ($x = 1.8$). The observation of the Dirac point indicates unique properties of graphene are well preserved in MoSe_2/G and $\text{MoSe}_{1.8}/\text{G}$. The shift of the Dirac point means indicates the n-type ($x = 2$) and p-type ($x = 1.8$) doping of graphene induced by the MoSe_x monolayer. The charge carrier mobilities can be extracted from the linear regimes on both sides of the current minimum using $\mu = (1/C_g) \cdot (\partial I_{\text{SD}} / \partial V_g)$, where C_g is the back gate capacitance ($1 \times 10^{-5} \text{ F/cm}^2$). Under the same measuring conditions, mobilities of MoSe_2/G (hole: $17.4 \text{ cm}^2\text{V}^{-1}\text{s}^{-1}$; electron: $22 \text{ cm}^2\text{V}^{-1}\text{s}^{-1}$) have comparable amounts with the graphene (hole: $41.1 \text{ cm}^2\text{V}^{-1}\text{s}^{-1}$; electron: $28 \text{ cm}^2 \text{V}^{-1}\text{s}^{-1}$), while as the reduction of x , mobilities of $\text{MoSe}_{1.8}/\text{G}$ lower to $0.24 \text{ cm}^2\text{V}^{-1}\text{s}^{-1}$ and $0.22 \text{ cm}^2\text{V}^{-1}\text{s}^{-1}$. The band structures of MoSe_x/G are calculated via First-principles as shown in Fig. 3b ($x = 2$) and Fig. 3d ($x = 1.8$). The band structure of MoSe_2/G appears like a simple sum of the isolated MoSe_2 monolayer and graphene. Although *Se*-vacancies introduce *Se*-defect-states in the bandgap of $\text{MoSe}_{1.8}/\text{G}$ (Fig. 3d), there is still a Dirac point in the bandgap of $\text{MoSe}_{1.8}/\text{G}$. This demonstrates that these heterostructures display similar properties with graphene near the

Fermi level, except for a subtle adjustment by the MoSe_x monolayer, which has a good agreement with FETs results. For $\text{MoSe}_{1.6}/\text{G}$ (Fig. 3e) and $\text{MoSe}_{1.4}/\text{G}$ (Fig. S10b) FETs, the V-shaped $I_{\text{SD}}-V_{\text{G}}$ characteristic disappears (replaced with a constant current ungovernable by the gate voltage), which can be explained by the calculated band structure in Fig. 3f. The characteristic Dirac point vanishes from K , displaced by hyperbolic-like lines. Meanwhile, the Fermi level of the heterostructure passes through the band, indicating the quasi-metallic behavior of MoSe_x/G ($x=1.6$ and 1.4). The conductivity (σ) of $\text{MoSe}_{1.6}/\text{G}$ ($\text{MoSe}_{1.4}/\text{G}$) is measured to be 160 S/m (32 S/m), which is far below Au (4.52×10^7 S/m). As σ is proportional to n (Density of electronic states near Fermi surface) [28] (Supplementary X), we can conclude n of $\text{MoSe}_{1.6}/\text{G}$ ($\text{MoSe}_{1.4}/\text{G}$) is only a hundred-thousandth (millionth) of Au.

To summarize, the FIB-writing process generates *Se*-vacancies with controllable density and distribution on the top atomic layer of the MoSe_2/G . *Se*-vacancies change the electronic properties of this heterostructure, and classify them into MoSe_x -modified graphene ($x=2$ and 1.8) and quasi-metallic MoSe_x/G ($x=1.6$ and 1.4) according to the presence of the Dirac point. Meanwhile, the work function of the heterostructure can be tailored by x from 5.2 eV to 4.85 eV. The tailored work function allows establishing a charge transfer region (CTR) or potential barrier for any charge carrier tunneling at the interface of MoSe_x -modified graphene and quasi-metal without the obstacles caused by the Klein tunneling, which paves the way to produce lateral 2D diodes on the MoSe_2/G heterostructure.

Rectification performance.

To provide direct evidence for the current suppression, a MoSe_2/G heterostructure is half irradiated between drain and source electrodes (D and S) to construct a 2D MoSe_x/G - MoSe_2/G rectifying diode. Figure 4a illustrates SEM (scanning electron microscope) and KPFM images of the heterostructure and the electrodes (D and S), in which the ultraviolet stands for the irradiated region. Different work functions induced by the FIB-writing cause a potential barrier between the irradiated and non-irradiated regions, and the carrier tunneling at

the barrier is detected through typical $|I_{SD}|-V_{SD}$ characteristics. Figure 4b shows rectification ratios ($r = I_{+20V}/I_{-20V}$) and $|I_{SD}|-V_{SD}$ curves for the $\text{MoSe}_x/\text{G}-\text{MoSe}_2/\text{G}$ diodes corresponding to $x = 2.0, 1.8, 1.6$ and 1.4 at room temperature. And the corresponding energy band diagrams are represented in Fig. 4c.

The $|I_{SD}|-V_{SD}$ characteristic of the $\text{MoSe}_{1.8}/\text{G}-\text{MoSe}_2/\text{G}$ is symmetric. Even there is a potential difference ($\Delta V = 0.1$) at the interface (Fig. 4c) of $\text{MoSe}_{2.0}/\text{G}$ and $\text{MoSe}_{1.8}/\text{G}$. It is because both $\text{MoSe}_{2.0}/\text{G}$ and $\text{MoSe}_{1.8}/\text{G}$ have the Dirac point, which enables the low-energy quasiparticles in the heterostructure to behave as massless Dirac fermions. According to the Klein tunneling effect, massless Dirac fermions have unlimited transport through potential barriers. While, the obvious current suppression appears in the $\text{MoSe}_{1.6}/\text{G}-\text{MoSe}_2/\text{G}$ ($r = 71$) and is further enhanced with $\text{MoSe}_{1.4}/\text{G}-\text{MoSe}_2/\text{G}$ ($r = 1.1 \times 10^4$), where the irradiated heterostructure is transferred to the quasi-metal without the Dirac point. The case of the $\text{MoSe}_{1.4}/\text{G}-\text{MoSe}_2/\text{G}$ contact is similar to the metal-graphene contact, in which a dipole layer is formed by the charge transfer process taking place at the interface (Fig. 4c). The charge transfer shifts the E_F of MoSe_2/G significantly, which bends the trace of the Dirac point and leads to a long screening length due to the small DOS around the E_F . Carriers in $\text{MoSe}_{1.4}/\text{G}$ are redistributed to screen the work function difference at the interface, and the screen length is proportional to $n^{-1/2}$ [28, 29]. Normally, the screen length in metal (like Au) is just a fraction of a nanometer due to the large value of n , which can be ignored [29]. But $\text{MoSe}_{1.4}/\text{G}$ as a quasi-metal has a very low n (six orders of magnitude less than Au). So the screen length of $\text{MoSe}_{1.4}/\text{G}$ is hundreds of nanometers, which is non-negligible. The key feature that originates from the long screen length in both $\text{MoSe}_{1.4}/\text{G}$ and MoSe_2/G is the p-n junction that appears near the $\text{MoSe}_{1.4}/\text{G}-\text{MoSe}_2/\text{G}$ contact.

Further experiments are performed to quantify the stability, filtering, and frequency responses of this $\text{MoSe}_{1.4}/\text{G}-\text{MoSe}_2/\text{G}$ rectifying diode. As displayed in Fig. 4d, performances of this diode are stable for the cycle number of 1×10^9 in air at room temperature. To detect the

filtering, MoSe_{1.4}/G-MoSe₂/G rectifying diode is connected to a rectifier circuit with a loading resistor of 10 k Ω (Fig. 4e), in which the positive/negative input voltage passes/stops with the rectification efficiency of 40.6%. Further changing the loading resistance to 40 k Ω , the rectification efficiency can increase to 75%, indicating the forward resistance of this rectifying diode is about 14 k Ω . To explore the frequency response, the MoSe_{1.4}/G-MoSe₂/G filtering diode is connected in parallel with a smoothing capacitor and a loading resistor, and simulated with a sinusoidal input. Figure 4f presents the measured voltage output in a rectifier configuration, in which the cutoff frequency is around 9.4 MHz.

Conclusion.

The FIB-writing has been demonstrated to be a high-efficient and automated way to manufacture lateral 2D diodes on graphene-based heterostructures. To demonstrate the superiority of this technique, Table 1 compares the performance of the MoSe_{1.4}/G-MoSe₂/G diode discussed in this work with previously reported ones. According to the different stacking way, 2D diodes can be classified into vertical and lateral heterojunction types. For the vertical diodes, devices possess the highest rectification ($10^2 \sim 10^6$), with a current density of $10^2 \sim 10^5$ A/cm² at the maximum reverse voltage. These are considered as the most practical potential 2D diodes [15, 16]. However, for the 2D lateral diodes realized through chemical or electrostatic doping, the rectification is $\sim 10^2$, and the current density is $\sim 10^2$ A/cm², thus requiring significant improvements. In this work, the MoSe_{1.4}/G-MoSe₂/G diode has a rectification of $\sim 10^4$ and a current density of $\sim 6.7 \times 10^4$ A/cm², representing comparable performance to 2D vertical diodes and evident advantages over other lateral diodes.

Experimental Methods

Sample preparation

The graphene and MoSe₂ monolayers were grown via chemical vapor deposition (CVD). The graphene and MoSe₂ were then transferred to the Si substrate one after the other through the wet-chemistry transfer process. A layer of PMMA was first spin-coated onto the substrate with MoSe₂ or graphene and then baked at 100°C for 5 min. Next, it was immersed into a 2-mol/L KOH solution for 2 hours to separate the PMMA/graphene (MoSe₂) from the substrate, and it was swilled fully with DI water. It was then collected on the target substrate and baked at 80°C for 2 hours. Finally, the film was immersed in acetone to remove the PMMA. The drain and source electrodes were fabricated via electron-beam lithography and evaporation (Au/SiO₂/Si, Au: 50 nm, SiO₂: 50 nm).

Ga ion beam writing

The writing of focused Ga⁺ ions was carried out using the FIB technique (model FEI START 400S). The acceleration voltage was 30 kV, while the beam current was 9.7 pA, 93 pA, and 0.79 nA.

Characterization

The fabricated devices were characterized using an optical microscope (Leica DM2700), and SEM (model FEI START 400S with accelerating voltage of 10kV), an AFM, and a KPFM (Bruker, Dimension Icon). The electrical and optoelectronic properties of the devices were measured via a Keithley 4200A-SCS at room temperature and room pressure. MoSe_x/G heterostructures used for Raman spectra and XPS spectra measurements were produced by CVD and transferred on copper nets. The power of the laser used in Raman spectra measurements was 1mW, and the wavelength was 473 nm.

Top-gated Field-Effect Transistors

A small droplet of saturated trifluorochloroethylene is dropped onto the top of FETs. The probe is inserted into the droplet above MoSe_x/G.

DFT calculations

First-principles calculations were performed using the density functional theory (DFT), adopting the plane-wave pseudopotential approach as implemented in the Vienna Ab initio Simulation Package (VASP) [32]. The electron-electron interaction in the calculations was described via the Perdew-Burke-Ernzerhof (PBE) functional under the generalized gradient approximation (GGA) [33]. The Van der Waals weak interaction between graphene and MoSe₂ was corrected via the Grimme method (DFT-D2). For the electron wave function, a plane wave with a cutoff energy of 500 eV was used. A vacuum region of 30 Å was applied in the *z*-direction to avoid interactions between adjacent images. The convergence threshold parameters for the optimization and the subsequent calculations were set to be 10⁻⁵ eV (energy) and 10⁻² eV/Å (force). K-point meshes of 5×5×1 were used in sampling the Brillouin zone for the 3×3-MoSe₂/4×4-graphene supercell of the heterostructure. All the atomic positions and lattice vectors were fully optimized using the conjugate gradient (CG) scheme without any restrictions.

Acknowledgments

The manuscript was written through the contributions of all authors. Y. Qu carried out the first principle calculation. H. Yin participated in the detailed charge transport experimental design. Y. Tan provided the original idea and is responsible for the organization of this work.

References

- (1) P. S. Peercy, *Nature* **2000**, *406*, 1023–1026.
- (2) X. Du, I. Skachko, A. Barker, E. Y. Andrei, *Nat. Nanotechnol.* **2008**, *3*, 491-495.
- (3) E. H. Hwang, S. Adam, S. D. Sarma, *Phys. Rev. Lett.* **2007**, *98*, 186806.
- (4) K. L. Seyler, P. Gong, P. Rivera, A. M. Jones, S. Wu, J. Yan, D. G. Mandrus, W. Yao, X. Xu, *Nat. Nanotech.* **2015**, *10*, 407–411.
- (5) D. Akinwande, C. Huyghebaert, C. Wang, M. I Sern, S. Goossens, L. J. L, H. P. Wong, F. H. L. Koppens, *Nature* **2019**, *573*, 507-518.
- (6) X. Duan¹, C. Wang, J. C. Shaw, R. Cheng, Y. Chen, H. Li, X. Wu, Y. Tang, Q. Zhang, A. Pan, J. Jiang, R. Yu, Y. Huang, X. Duan, *Nat. Nanotech.* **2014**, *9*, 1024–1030.
- (7) A. Allain, J. H. Kang, K. Banerjee, A. Kis, *Nat. Mater.* **2015**, *14*, 1195–1205.
- (8) L. Wang, I. Meric, P. Y. Huang, Q. Gao, Y. Gao, H. Tran, T. Taniguchi, K. Watanabe, L. M. Campos, D. A. Muller, J. Guo, P. Kim, J. Hone, K. L. Shepard, C. R. Dean *Science* **2013**, *342*, 614–617.
- (9) L. Ci, L. Song, C. Jin, D. Jariwala¹, D. Wu, Y. Li, A. Srivastava¹, Z. F. Wang, K. Storr, L. Balicas, F. Liu, P. M. Ajayan. *Nat. Mater.* **2010**, *9*, 430-435.
- (10) K. W. Urban, *Nat. Mater.* **2011**, *10*, 165-166.
- (11) X. Li, X. Wang, L. Zhang, S. Lee, H. Dai, *Science* **2008**, *319*, 1229-1232.
- (12) Y. Zhang, T. Tang, C. Girit, Z. Hao, M. C. Martin, A. Zettl, M. F. Crommie, Y. R. Shen, F. Wang *Nature* **2009**, *459*, 820-823.
- (13) F. Yavari, C. Kritzing, C. Gaire, L. Song, H. Gulapalli, T. B. Tasciuc, P. M. Ajayan, N. Koratkar, *Small* **2010**, *6*, 2535-2538.
- (14) D. Hsieh, Y. Xia, D. Qian, L. Wray, J. H. Dil, F. Meier, J. Osterwalder, L. Patthey, J. G. Checkelsky, N. P. Ong, A. V. Fedorov, H. Lin, A. Bansil, D. Grauer, Y. S. Hor, R. J. Cava, M. Z. Hasan, *Nature* **2009**, *460*, 1101-1105.
- (15) D. Neumaier, S. Pindl, M. C. Lemme, *Nat. Mater.* **2019**, *18*, 525-529.

- (16) L. Lin, H. L. Peng, Z. F. Liu, *Nat. Mater.* **2019**, *18*, 520-524.
- (17) F. Watt, A. A. Bettiol, J. A. van Kan, E. J. Teo, M. B. H. Breese, *Int. J. Nanosci.* **2005**, *4*, 269-286.
- (18) J. Melngailis, *J. Vac. Sci. Technol. B* **1987**, *5*, 469-495.
- (19) J. P. Thiruraman, P. M. Das, M. Drndić, *Adv. Funct. Mater.* **2019**, *29*, 1904668.
- (20) Y. R. Liu, Z. B. Gao, M. Chen, Y. Tan, F. Chen, *Adv. Funct. Mater.* **2018**, *28*, 1805710.
- (21) L Y. R. Liu, Z. B. Gao, Y. Tan, F. Chen, *ACS Nano* **2018**, *12*, 10529-10536.
- (22) J. C. Bernède, *Appl. Surf. Sci.* **171**, 15-20 (2001).
- (23) Abdallah, A. W. & Nelson., A. E. Characterization of MoSe₂ (0001) and ion-sputtered MoSe₂ by XPS. *J. Mater. Sci.* **2005**, *40*, 2679-268.
- (24) Y. Yang, S. Wang, J. Zhang, H. Li, Z. Tang, X. Wang, *Inorg. Chem. Front.* **2015**, *2*, 931-937.
- (25) B. Xia, T. Wang, X. Jiang, T. Zhang, J. Li, W. Xiao, P. Xi, D. Gao, D. Xue, J. Ding, *ACS Energy Lett.* **2018**, *3*, 2167-2172.
- (26) M. M. Samani, L. Liang, A. Oyedele, Y. Kim, M. Tian, N. Cross, K. Wang, M. Lin, A. Boulesbaa, C. M. Rouleau, A. A. Poretzky, K. Xiao, M. Yoon, G. Eres, G. Duscher, B. G. Sumpter, D. B. Geohegan, *Nano Lett.* **2016**, *16*, 5213–5220.
- (27) J. A. Appelbaum, D. R. Hamann, *Phys. Rev. Lett.* **1974**, *32*, 225-228.
- (28) J. M. Zaiman, PRINCIPLES OF THE THEORY OF SOLIDS. (Cambridge University Press, Cambridge, U.K., **1976**).
- (29) K. Nagashio, A. Toriumi, *Jpn. J Appl. Phys.* **2011**, *50*, 070108.
- (30) Ke, J. CONCISE HANDBOOK OF ELECTRONIC COMPONENTS (Higher Education Press, Shanghai, **1991**).
- (31) A. Zhang, Q. Zhou, C. Yang, Y. Shi, W. Chen, Z. Li, B. Zhang, *Nanoscale Res. Lett.* **2019**, *14*, 1-6.

- (32) H. Liu, N. Han, J. Zhao, *RSC Adv.* **2015**, *5*, 17572-17581.
- (33) G. Gui, J. Li, J. Zhong, *Phys. Rev. B* **2008**, *78*, 075435.
- (34) C. Liu, W. Ma, M. Chen, W. Ren, D. Sun, *Nat. commun.* **2019**, *10*, 4873.
- (35) W. J. Yu, Z. Li, H. Zhou, Y. Chen, Y. Wang, Y. Huang, X. Duan, *Nat. Mater.* **2013**, *12*, 246-252.
- (36) G. Dastgeer, M. F. Khan, G. Nazir, A. M. Afzal, S. Aftab, B. A. Naqvi, J. Cha, K. Min, Y. Jamil, J. Jung, S. Hong, J. Eom, *ACS Appl. Mater. Inter.* **2018**, *10*, 13150-13157.
- (37) R. Cheng, D. Li, H. Zhou, C. Wang, A. Yin, S. Jiang, Y. Liu, Y. Chen, Y. Huang, X. Duan, *Nano lett.* **2014**, *14*, 5590-5597.
- (38) Y. Deng, Z. Luo, N. J. Conrad, H. Liu, Y. Gong, S. Najmaei, P. M. Ajayan, J. Lou, X. Xu, P. D. Ye, *ACS Nano* **2014**, *8*, 8292-8299.
- (39) M. Li, Y. Shi, C. Cheng, L. Lu, Y. Lin, H. Tang, M. Tsai, C. Chu, K. Wei, J. He, W. Chang, K. Suenaga, L. Li, *Science* **2015**, *349*, 524-528.
- (40) H. G. Ji, P. S. Fernández, D. Yoshimura, M. Maruyama, T. Endo, Y. Miyata, S. Okada, H. Ago, *Adv. Mater.* **2019**, *31*, 1903613.
- (41) S. Jia, Z. Jin, J. Zhang, J. Yuan, W. Chen, W. Feng, P. Hu, P. M. Ajayan, J. Lou, *small* **2020**, *16*, 202002263.

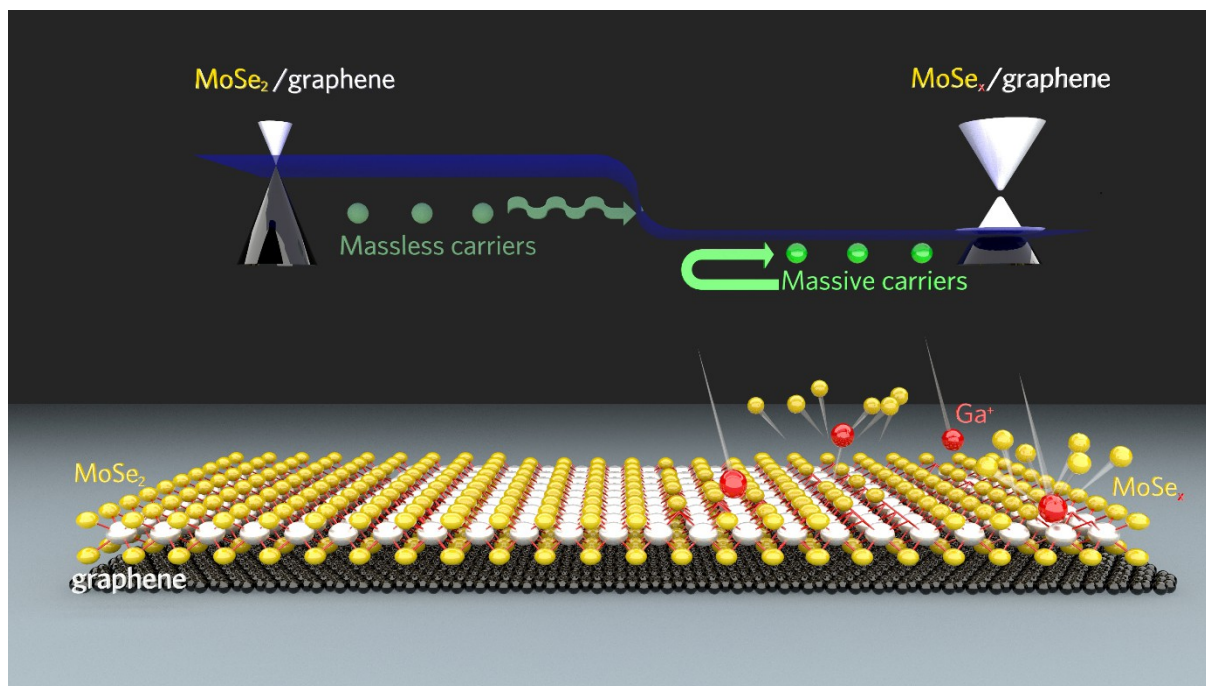


Figure 1. Schematic diagram of the FIB-writing process.

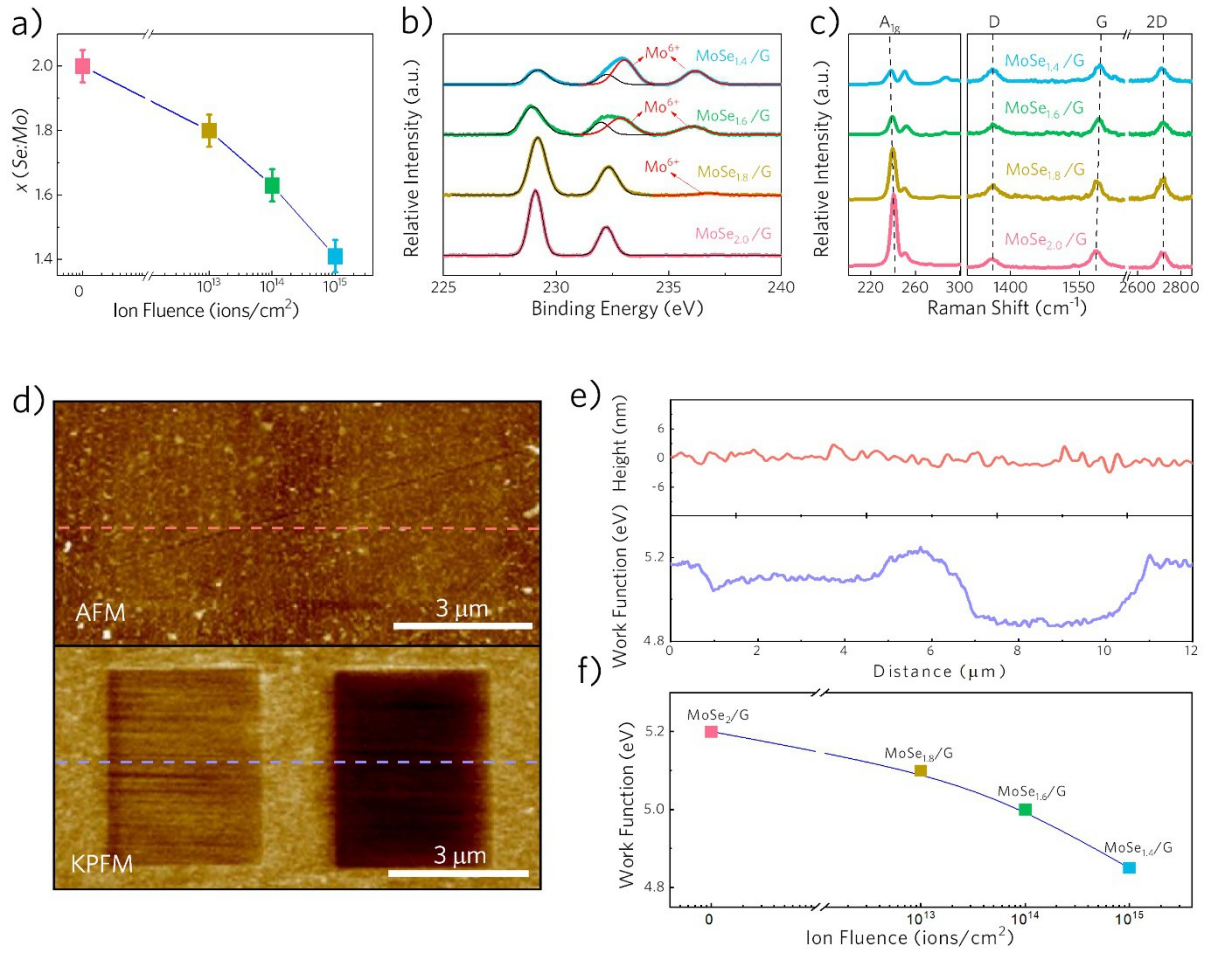


Figure 2. Defect-engineered MoSe_x/G heterostructure. **(a)** Evolution of the stoichiometric ratio $Se:Mo$ as a function of the ion fluence of the Ga^+ ion beam. **(b)** XPS spectra of MoSe_x/G at Mo-3d. **(c)** Raman spectra of MoSe_x/G. (A_{1g} peak for MoSe_x; D, G, and 2D peaks for graphene) **(d)** AFM and KPFM images of the heterostructures written in the rectangular shapes corresponding to MoSe_{1.8}/G and MoSe_{1.4}/G. **(e)** Thickness/work-function corresponding to the pink/purple dashed lines in **(d)**. **(f)** The measured work function of MoSe_x/G.

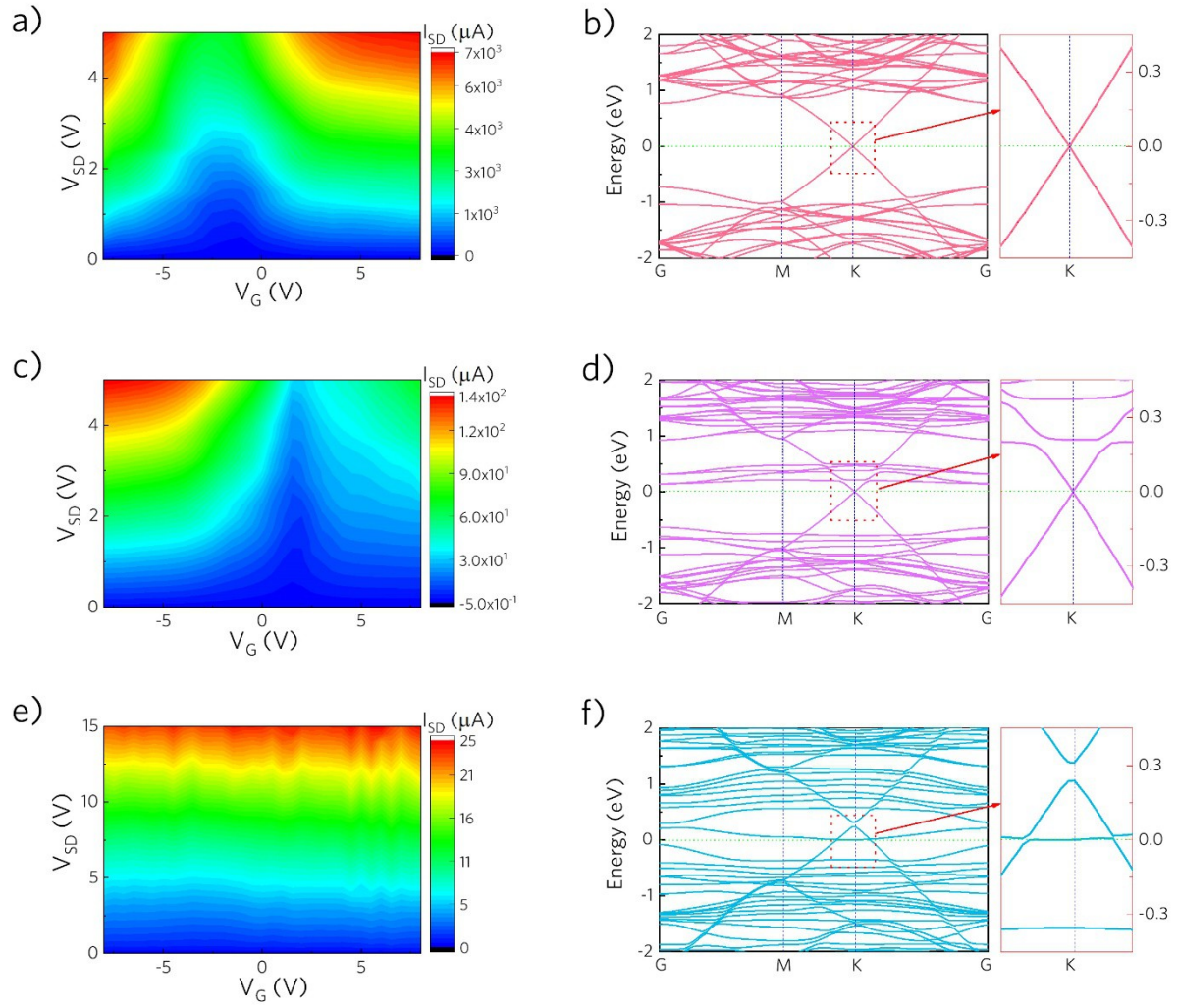


Figure 3. Calculated electronic structure of the MoSe_x/G heterostructure. Gate dependence (V_{G}) of the drain current $I_{\text{SD}}-V_{\text{SD}}$ of MoSe_2/G (a), $\text{MoSe}_{1.8}/\text{G}$ (c), and $\text{MoSe}_{1.6}/\text{G}$ (e). Calculated electronic structures of $\text{MoSe}_{2.0}/\text{G}$ (b), $\text{MoSe}_{1.78}/\text{G}$ (d), and $\text{MoSe}_{1.56}/\text{G}$ (f). The Fermi level is set to 0.

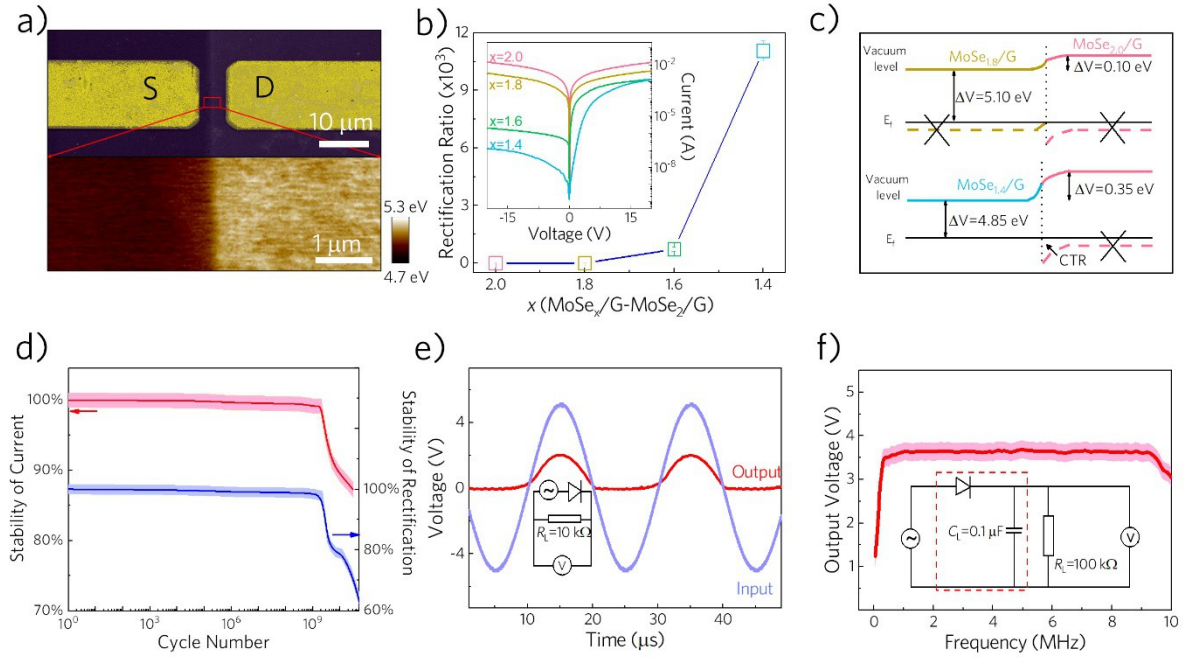


Figure 4. Rectifying diodes based on the MoSe _{x} /G heterostructure. **(a)** SEM (top) and KPFM (bottom) images of the MoSe_{1.4}/G rectifying diode. **(b)** Evolution of the rectification ratio as a function of x . The inset image is $|I_{SD}|$ - V_{SD} characteristics of the rectifying diodes constructed with MoSe_{2.0}/G, MoSe_{1.8}/G, MoSe_{1.6}/G, and MoSe_{1.4}/G, at room temperature. **(c)** Corresponding energy band diagrams of MoSe_{1.8}/G-MoSe₂/G and MoSe_{1.4}/G-MoSe₂/G. **(d)** The variation ratio of the current and rectification (at $V_{SD} = +10$ V) of the rectifying diode along with the cycle number. **(e)** Time-resolved input and output voltages of the rectifier circuit. The loading resistor in this circuit is 10 k Ω . **(f)** Frequency-resolved output voltage in the rectifier configuration. All measurements were taken in air at room temperature.

Table 1. Comparison of 2D diodes in literature.

<i>Heterojunction type</i>	<i>Layer structure</i>			<i>Ref.</i>
Vertical diodes	Ge/G/Si	1.0×10^6 at 5 V ^a 1.0×10^5 at 2 V	6.9×10^2 A/cm ² at 5 V ^a 21 A/cm ² at 2 V	[34]
	G/MoS ₂	1.5×10^3 at 4 V ^a 2.0×10^2 at 2 V	3.5×10^5 A/cm ² at 4 V ^a 1.0×10^5 A/cm ² at 2 V	[35]
	BP ^b /WS ₂	2.0×10^3 at 5 V ^a 1.0×10^2 at 2 V	2.0×10^2 A/cm ² at 5 V ^a 20 A/cm ² at 2 V	[36]
	WSe ₂ /MoS ₂	1.0×10^2 at 2 V ^a	50 A/cm ² at 2 V ^a	[37]
	BP ^b /MoS ₂	1.0×10^3 at 2 V ^a	1 A/cm ² at 2 V ^a	[38]
Lateral diodes	WSe ₂ /MoS ₂	1.0×10^2 at 2 V ^a	33 A/cm ² at 2 V ^a	[39]
	WSe ₂ /WSe ₂	1.0×10^2 at 5 V ^a 10 at 2 V	0.7 A/cm ² at 5 V ^a 0.02 A/cm ² at 2 V	[40]
	WSe ₂ /MoSe ₂	1.0×10^2 at 5 V ^a ~5 at 2 V	5 A/cm ² at 5 V ^a 0.15 A/cm ² at 2 V	[41]
	MoSe _{1.4} /G	1.1×10^4 at 20 V ^a 1.0×10^2 at 2 V	2.4×10^4 A/cm ² at 20 V ^a 6.5×10^2 A/cm ² at 2 V	This work

^a The maximum reverse voltage

^b Black phosphorus